Materials Today Bio 28 (2024) 101195

Contents lists available at ScienceDirect

Materials Today Bio

journal homepage: www.journals.elsevier.com/materials-today-bio

Myotube formation on micropatterns guiding by centripetal cellular motility and crowding

Jie Gao [a,1], Xiang Sun [b,1], Yanning Ma [a,c,1], Wen Qin [a], Jin Li [d], Zuolin Jin [a], Jun Qiu [e,**], Hao Zhang [a,*]

[a] State Key Laboratory of Oral & Maxillofacial Reconstruction and Regeneration, National Clinical Research Center for Oral Diseases, Shaanxi Clinical Research Center for Oral Diseases, Department of Orthodontics, School of Stomatology, The Fourth Military Medical University, Xi'an, 710032, China
[b] Department of Stomatology, The First Hospital of Yulin, Yulin, 719000, China
[c] Shanxi Medical University School and Hospital of Stomatology, Taiyuan, 030001, China
[d] Department of Infectious Diseases, The First Affiliated Hospital of Army Medical University, Chongqing, 400038, China
[e] State Key Laboratory of Oral & Maxillofacial Reconstruction and Regeneration, National Clinical Research Center for Oral Diseases, Shaanxi Clinical Research Center for Oral Diseases, Department of Operative Dentistry and Endodontics, School of Stomatology, The Fourth Military Medical University, Xi'an, 710032, China

ARTICLE INFO

Keywords:
Micropattern
Substrate rigidity
Myotube
Cell crowding
Migration

ABSTRACT

The physical microenvironment, including substrate rigidity and topology, impacts myoblast differentiation and myotube maturation. However, the interplay effect and physical mechanism of mechanical stimuli on myotube formation is poorly understood. In this study, we utilized elastic substrates, microcontact patterning technique, and particle image velocimetry to investigate the effect of substrate rigidity and topological constraints on myoblast behaviors. Our findings suggested the interplay of substrate stiffness and cellular confinement improved the myotube formation by inducing centripetal cellular motility. These results shed light on the impact of the topological substrate on myoblast differentiation and emphasize the critical role of asymmetrical cell motility during this process, which is highly correlated with cell movement and crowding. Our research provides insights into the intricate interplay between substrate properties, cell motility, and myotube formation during myogenesis. Understanding these mechanisms could trigger tissue engineering strategies and therapies to enhance muscle regeneration and function.

1. Introduction

Striated muscles acquire mature rods of highly aligned myofibers to generate sufficient contractile forces. Thus, the formation of contractile myotubes serves as a crucial indicator of myofiber generation during myogenesis, a process intricately intertwined with multiple complex mechanisms, such as cell growth and the eventual fusion of myogenic progenitor cells into striated multinucleated myotubes. These myotubes then further assemble into well-organized fibrous structures that span the entire muscle length, forming a cohesive and functional unit [1]. This process is often thought to be regulated by biochemical molecules such as myogenic regulatory factors (MyoD, Myf5, and Mrf4) [2], growth factors (TGF-β1, FGF-2, and IGF-1) [3–6], and inflammatory cytokines (TNF-α and IL-6) [7,8]. Beyond chemical regulators, recent studies have elucidated the fundamental significance of physical environmental cues, such as substrate rigidity and external forces, in synergistically facilitating myotube formation alongside chemical inducers, thereby contributing to a more comprehensive understanding of myogenesis [9,10]. For instance, by culturing C2C12 myoblasts on collagen strips attached to hydrogel substrates of varied rigidity, subsequent fusion into myotubes occurs independent of substrate flexibility [11]. Such fusion and striation of myoblasts are highly correlated with their increased adhesion and intracellular contractility when cultured on a stiff elastic substrate. Other studies reported that mechanical forces could influence myotube formation and maturation in vitro. Kumar et al. reported that biaxial stretching of myoblasts significantly increased their proliferation and inhibited differentiation into myotubes through a nuclear factor-kappa B-dependent mechanism [12]. In addition, using a

* Corresponding author.
** Corresponding author.
E-mail addresses: qiujun@fmmu.edu.cn (J. Qiu), zhanghao@fmmu.edu.cn, 120904448@qq.com (H. Zhang).
[1] Authors contributed equally to this work.

https://doi.org/10.1016/j.mtbio.2024.101195
Received 28 February 2024; Received in revised form 5 August 2024; Accepted 8 August 2024
Available online 9 August 2024

uniaxial mechanical stretcher, Vandenburgh et al. found that mechanical force increases the expression of myotube-related protein through a cyclooxygenase-dependent mechanism [13]. Another study by Pennisi et al. compared the distinct impacts of uniaxial and equibiaxial 15 % cyclic tensile stretch (0.5 Hz) on myogenic differentiation [14]. According to their observation, uniaxial stretch drives C2C12 differentiation, while equibiaxial stretch does not favor the differentiation process.

In addition to substrate rigidity and forces, recent findings have demonstrated that topological constraints also influence myotube formation. Specifically, they enhance cell-extracellular matrix (ECM) interactions and serve as guiding factors for myoblast differentiation. In these studies, microfabrication and microfluidics techniques have been widely used to create topological features, including adhesive micropatterns, strait grooves, micropillars, wrinkles, and fibrous structures [15]. For example, ultraviolet (UV)-activated methoxy polyethylene glycol (mPEG)-scission reaction was used to micropattern ECM protein on glass slides. In particular, the myoblast fusion and differentiation were induced by the force gradient correlated to the topological defects on the micropatterns [16]. In another study, substrates coated with CH3 molecules for fibronectin adsorption have been shown to promote the alignment of C2C12 myoblasts and MC3T3-E1 osteoblasts in vitro [17]. This discovery adds further depth to our comprehension of the intricate mechanisms underlying the process of myogenesis. While most studies concur that either substrate rigidity or topological constraints can regulate myotube formation, the combined effect of these two stimuli on myotube formation is less known.

To answer this question, we employed a combination of elastic gels microcontact patterning (μCP), traction force microscopy (TFM), and particle image velocimetry (PIV) to investigate the impact of substrate rigidity and topological constraints on various myoblast behaviors, including spreading, contraction, migration, and differentiation. Myoblast spreading, elongation, and migration were found to be contingent upon substrate rigidity, while the presence of topological constraints enhanced cell elongation, alignment, and migration on stiff substrates. Specifically, the topological constraints accelerated cell elongation and migration along the periphery of gel micropatterns (μPatterns), inducing an asymmetrical crowding effect within the cell populations at the core. Through PIV analysis, it was demonstrated that cell motility at the periphery generated force gradients along the μPatterns, leading to the compaction of central cells, a phenomenon evident by the crowding effects on cellular nuclei. Remarkably, this crowding event was closely associated with myotube formation on the μPatterns. In summary, our study revealed the biophysical implications of myotube formation on topological substrates, shedding light on the pivotal role of asymmetrical cell motility in this process, which correlates significantly with force transmission and crowding dynamics.

2. Results

2.1. Myoblast adhesion, proliferation, and contraction favor stiff gel substrate

Microcontact patterning (μCP) is a well-established technique used for confining cell adhesive boundaries [18,19]. To regulate both cellular adhesive geometry and substrate rigidity, we integrated micropatterning with a commercial acrylamide (PA) hydrogel with hydroxyl groups, allowing the protein and biomolecules to adhere to the hydrogel surface. This is an important step for subsequent protein patterning by using a polydimethylsiloxane (PDMS) stamp[20–22]. To examine the effects of geometric constraints and substrate rigidity on the behavior of myoblasts, we micropatterned adhesive fibronectin on the surface of hybrid hydroxyl-functionalized PA gels using μCP (Fig. 1A). As previous work showed that the pattern width, ranging from 65 to 85 μm that approximated as the range of muscle fiber diameter in vivo, played a major role in guiding myoblast differentiation [23]. On the contrary, the length of the lane pattern is much less influential than its width. We, therefore, defined 72μm × 180 μm as our protein pattern dimension. In particular, the rigidity of PA-gels could be tuned by varying the ratio of monomers and crosslinkers. Cells primarily sense mechanical signals from the mechanical characteristics of their surrounding matrix.

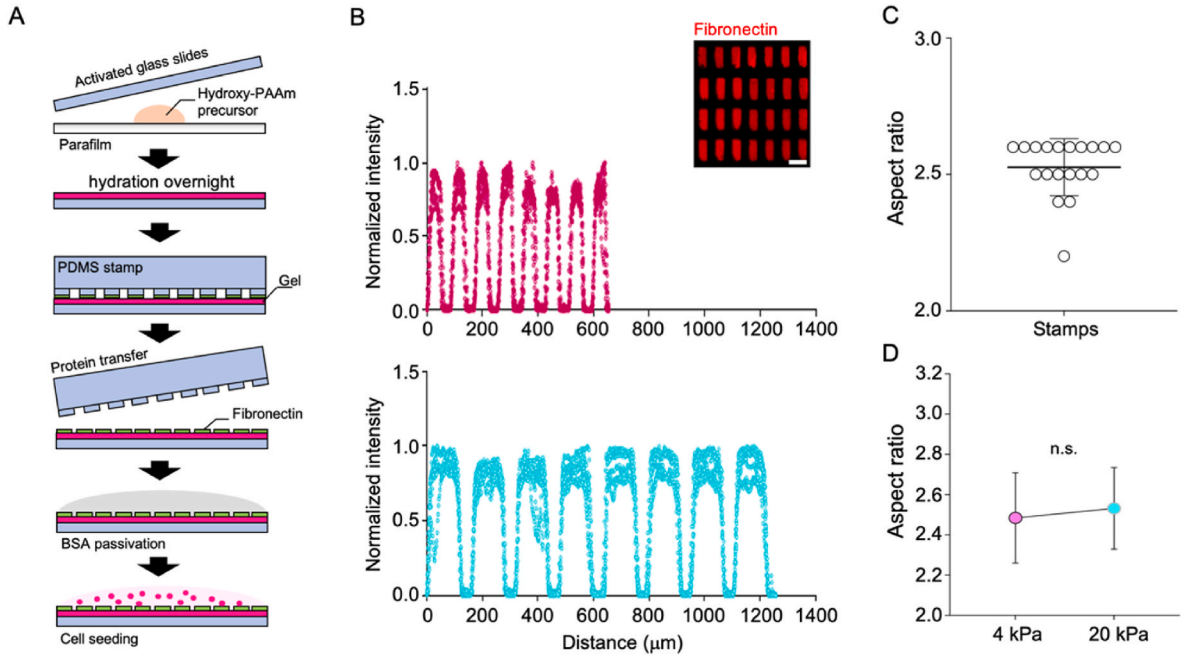

Fig. 1. Characterization of μPatterns. A) Illustration of the fabrication method for hydroxy-PA gels with fibronectin μPatterns. B) Normalized intensity profile of the linescan along the width (up panel) and length (bottom panel) of eight μPatterns. The inset panel represents the confocal images of μPatterns (fibrinogen–Cy3), indicating homogeneous and high throughput characteristics of the μCP method (n = 7 μPatterns, N = 3 experiments). Scale bars, 100 μm. C) Aspect ratio of the PDMS stamps (n = 19 μPatterns, N = 3 experiments). D) Aspect ratio characterized from the confocal microscopy images of μPatterns on 4 kPa and 20 kPa hydrogels. The Kolmogorov–Smirnov test was used for data analysis. Data are presented as mean values ± s.d. (n.s., no significant differences).

Notably, it has been reported that the elastic modulus of human skeletal muscle is 24.7 ± 3.5 kPa [24]. Thus, we used a stiff (~20 kPa) gel to mimic the in vivo mechanical microenvironment and two other softer (~4 kPa and ~12 kPa) gels as control. The local rigidity of PA-gels was tested using atomic force microscopy (AFM) (Supplementary Fig. 1A), which is consistent with previous results [25]. Since cells can only adhere and grow on surfaces with FN, ideally, we could control the cell-spreading area by tuning ECM topology. To demonstrate this hypothesis, we first characterized the μPattern shape using FN mixed with fibrinogen–Cy3. Before processing patterning by using a PDMS stamp, the gel was immersed either in PBS or a culture medium to obtain full hydration (Supplementary Fig. 2). The fluorescent images showed an FN array of rectangular shapes, which was further verified by plotting the intensity of fibrinogen as a function of μPattern dimensions (line-scans) (Fig. 1B). To assess whether signals of Cy3 fluorophores on both 4 kPa and 20 kPa gels accurately reflect the shape of μPatterns, we compared either the aspect ratio (after 24 incubation with culture medium) or the absolute size parameters of μPatterns from fluorescent images with the shape of PDMS stamp arrays (Fig. 1C and Supplementary Fig. 1B). The average aspect ratio of 4 kPa (2.48) and 20 kPa gels (2.53) was consistent with the aspect ratio of PDMS stamp arrays (2.52) (Fig. 1C–and D). Similarly, the difference in width and length between PDMS stamps and μPatterns on the gels was not observed. These results indicated that, in our system, the shape of μPattern is independent of gel rigidity and μCP process.

Hydrogels are porous fluid-saturated materials that can swell in water. We characterized the PA-gel swelling property and found equilibrium swelling of gels after the first 30 min immersion in PBS (Supplementary Fig. 2A). Notably, the PA-gel swelling property is related to the crosslinker concentration. As we performed the μCP on gels after they reached full swollen state (overnight hydration in PBS), we assumed that the shape of μPatterns was independent of the μCP. To test this hypothesis, we characterized the size of μPatterns on gels before and after a second-round of hydration in PBS for 24 h. We did not observe any shape changes of μPatterns on gels before and post-hydration (Supplementary Figs. 2C and D). This result suggested that, in our system, the swelling property of PA-gels is not an influencer of the μPattern shape.

As cells can sense substrate rigidity through activation of the RhoA pathway [26], resulting in the recruitment of focal adhesion (FA) related proteins at the cell periphery, we investigated whether stiff substrate positively affects myoblast adhesive behaviors. We performed immunostaining for vinculin, a well-known marker for matured FAs [27], on myoblasts cultured on non-patterned substrates with different rigidity for 24 h. To evaluate the difference in cell behaviors between normal petri dishes and PA gels, a tissue culture polystyrene group (TCPS), which rigidity is around ~ MPa, was also performed in these experiments. Remarkably, myoblasts exhibited the formation of larger FA islands (Fig. 2A–C) and thicker stress fibers when increasing the substrate rigidity, suggesting the enhancement of cell adhesion and spreading behavior triggered by the mechanical environment. Therefore, we explored whether cell spreading is sensitive to substrate rigidity. We assessed cellular circularity and spreading area at 6 h after cell seeding (Fig. 2D–G). As anticipated, myoblasts exhibited an increase in spreading area and elongation when cultured on the stiffer substrate, implying downstream effects of enhanced cell adhesion and maturation of the cytoskeleton network. Thus, we performed immunostaining for the actin network in myoblasts cultured on 4 kPa and 20 kPa μPatterns. Subsequently, we employed OrientationJ to quantify the local orientational distribution of stress fibers. Notably, in cells on the 20 kPa substrate, stress fibers displayed a high degree of alignment along the longitudinal axis of the μPatterns (Supplementary Fig. 3), highlighting the significant impact of substrate rigidity on actin reorganization. To assess the influence of substrate rigidity on cell proliferation, we generated a plot illustrating the number of nuclei in cells cultured on 4 kPa and 20 kPa μPatterns over time (Fig. 2G). The results indicated an elevated proliferation rate of cells cultivated on a substrate with higher rigidity, aligning with previous findings [28].

Another notable consequence of cellular mechanosensing is the adaptation of intracellular traction forces in response to mechanical stimuli. The cell could generate forces and deform the hydrogel substrate by intracellular contraction of cytoskeletons. To measure such forces, TFM was established to map the displacement fields of embedded small beads [29,30]. This deformation field is used to calculate TFM exerted at each contact point between a cell and substrate. Here, we conducted TFM measurements of myoblasts cultured on substrates with different rigidity. We observed that myoblasts exerted lower traction forces on soft gel substrates (~4 and ~12 kPa), whereas the stiff substrates (~20 kPa and TCPS) induced a more elongated and contractile phenotype (Fig. 2H). Together, these findings suggest a strong correlation between cell contractility and elongation, potentially governed by the organization of the actin cytoskeleton and maturation of focal adhesions guided by the RhoA signaling pathway [31]. Subsequently, we plotted the cellular traction force over time, starting from the moment the cells adhered fully to the substrates (Fig. 2I). Interestingly, the traction force of cells on 20 kPa substrates initially exceeded that of cells on 4 kPa substrates, and it increased over time until reaching a plateau after 30 min of culturing. We designated the amplitude of traction force at this plateau as the maximum traction. We also tested the maximum traction of cells cultured on 12 kPa and TCPS substrate (Supplementary Fig. 4). Interestingly, there was no significant difference in the maximum cellular tensile force between the 20 kPa and TCPS groups, indicating that the efficiency of RhoA activation reached a plateau in response to increasing of substrate rigidity. This should be confirmed in the further study. Collectively, these results suggest that substrate rigidity positively regulates cell adhesion, spreading, and contraction through the formation of matured focal adhesions and the reorganization of actin networks.

2.2. *Topological constraints accelerated myoblast spreading and contraction at peripheral zones of μPatterns*

Considering that the μPattern area significantly exceeds the cell spread area in our model, we explored the potential dependence of cell spreading behaviors on μPattern boundaries. Interestingly, we observed two specific regions of 20 kPa μPatterns regarding to the differential of cell elongation. At the periphery region of μPatterns (~25 μm away from the pattern edge, Supplementary Fig. 5), exhibited a greater degree of elongation compared to those in the central zones, suggesting the presence of distinct cytoskeletal tension during cell spreading (Fig. 3A and B and Supplementary Fig. 6). This differential could be a potential consequence that induces the crowding effect of central cells. Furthermore, the formation of myotubes necessitates cell populations attaining confluence, a condition tightly linked to cell density. To address this, we performed immune-labeling of myoblast nuclei on μPatterns over time in culture. The results revealed an increase in cell density, specifically at the central region of μPatterns with higher stiffness, whereas such a trend was not observed in the 4 kPa substrate groups (Fig. 3C, left panel). This result suggests the existence of an asymmetric distribution of cell populations influenced by substrate rigidity. Moreover, quantitative analysis showed that cell intensity was significantly higher at the central region of 20 kPa μPatterns within 3-day culturing, as evidenced by the heatmap representing the normalized intensity of DAPI-labeled nuclei (Fig. 3C, right panel). These collective results indicate that the crowding of cells at the central region of μPatterns is contingent upon the rigidity of the substrate. The elongation of the cell is considered to exhibit a consistent correlation with intracellular traction forces. Therefore, we normalized the average maximum traction force exerted by cells in various zones of the μPattern (Fig. 3C and D). Intriguingly, the resulting heatmap distinctly revealed a progressive escalation of cell maximum traction force from the central to the peripheral zones of 20 kPa μPatterns, a trend conspicuously absent in the case of cells on 4 kPa

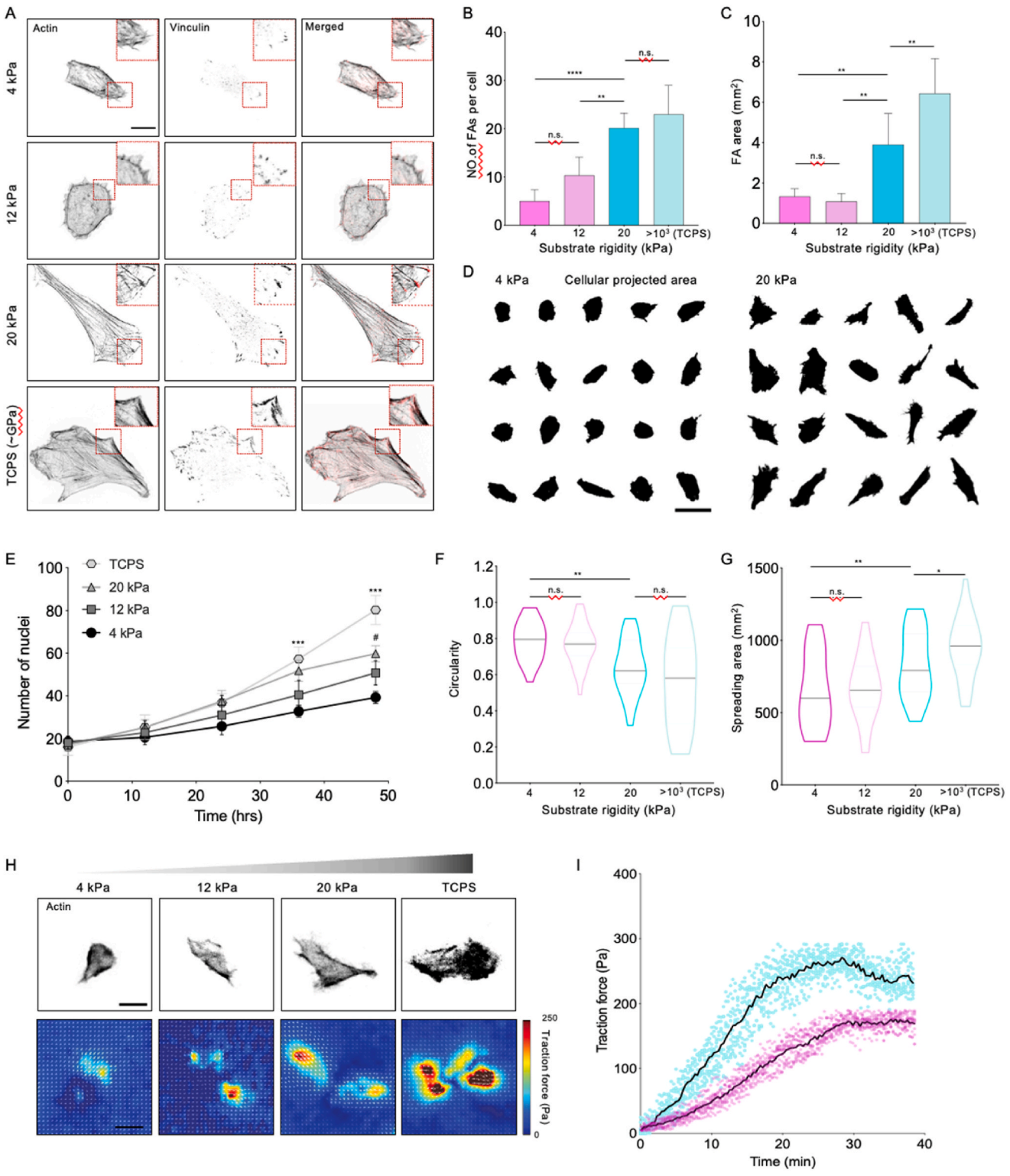

Fig. 2. Substrate rigidity enhanced cell adhesion, elongation, and contractility. A) Immunostaining images of actin and vinculin of myoblasts cultured on non-patterned substrates with different rigidity. Scale bars, 5 μm. B) Quantification of the number of vinculin islands per cell (n = 10 cells, N = 3 experiments). C) Quantification of the area of vinculin islands per cell (n = 11 cells, N = 3 experiments). D) Cell outlines of randomly selected myoblasts (after 2 h seeding) on 4 kPa and 20 kPa hydrogel substrates. Scale bars, 20 μm. E) Circularity of myoblasts on different substrates (n = 13 cells, N = 3 experiments). F) Spreading areas of myoblasts on different substrates (n = 13 cells, N = 3 experiments). G) The number of nuclei was plotted as a function of culturing times after fully cell spreading. Cellular nuclei were labeled by Hoechst 33342 and counted from timelapse. H) Representative microscopy images (left panel) and corresponding traction force maps of myoblasts spread on different substrates. Scale bar, 10 μm. I) Traction force plotted as a function culturing time on different substrates (n = 13 cells, N = 2 experiments). The one-way ANOVA with Tukey post-hoc testing was used for data analysis. Data are presented as medians in violin graph (solid line) (*n.s.*, no significant differences, $*p < 0.05$, $**p < 0.01$, and $***p < 0.001$).

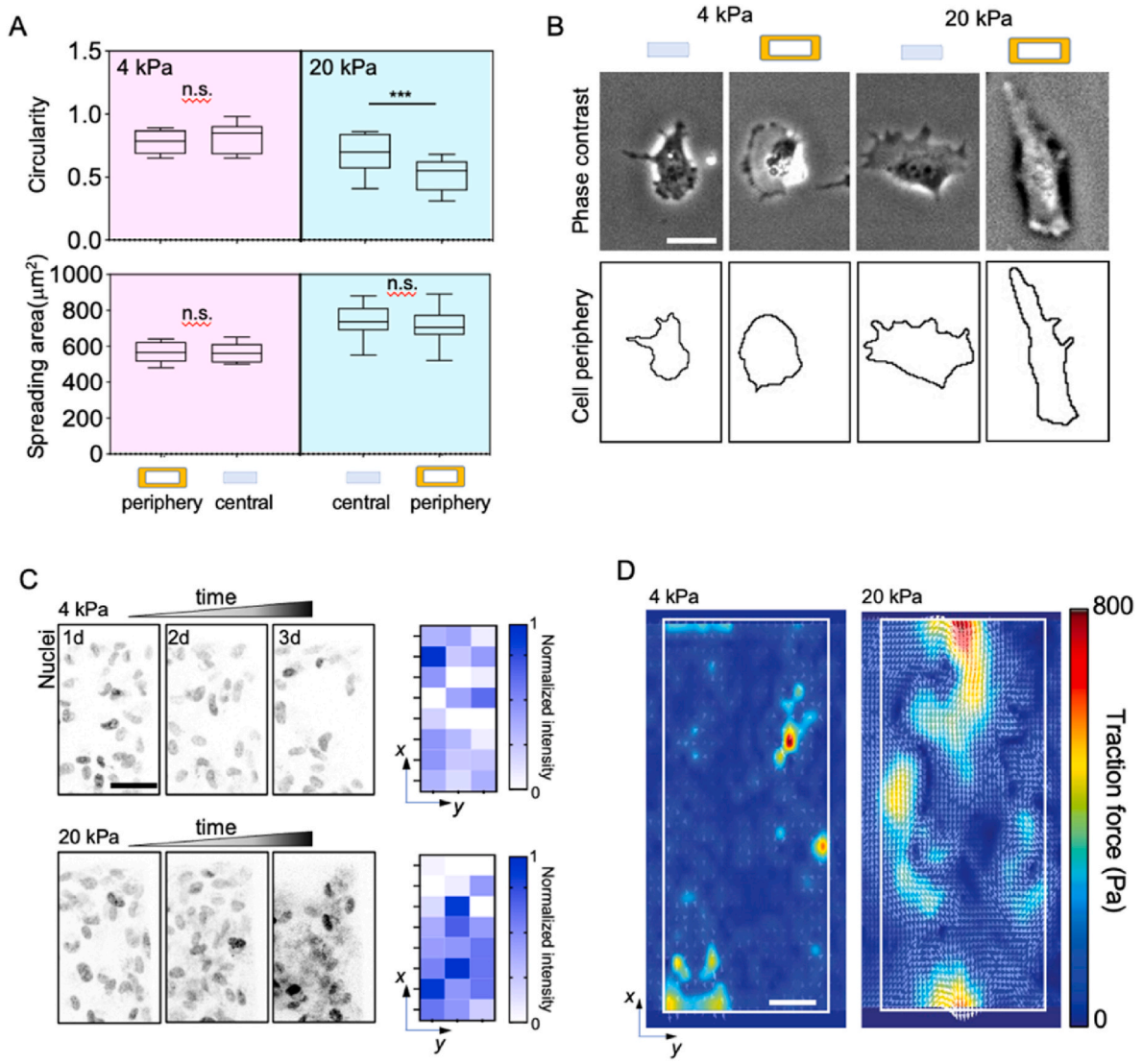

Fig. 3. Cells exhibit an increased spreading, elongation, and contraction at the peripheral regions of stiff μPatterns. A) Morphological analysis of individual myoblasts on both the specific zones (according to Supplementary Fig. 5) of 4 kPa and 20 kPa μPatterns (n = 13 cells, N = 3 experiments). B) Representative images of individual cells that locating at different regions of μPatterns. The bottom panel represents the related binary cell boundary segmented by ImageJ software. Scale bars, 10 μm. C) The myoblasts labeled with Hoechst 33342 on the central region of μPatterns indicated the cell density within 3-day culturing (n = 4 patterns, N = 2 experiments). The right panel revealed the heatmap of cell density on day 3 of culturing. Scale bars, 10 μm. D) The traction force heatmaps of cell populations at 4 kPa and 20 kPa μPatterns on day 3 of culturing. The solid frame indicated the boundary of μPatterns. Scale bars, 20 μm.

μPatterns. These findings showed that on μPatterns, cell contractility, and migration exhibit a region-specific distribution characteristic.

2.3. Topological constraints regulate the cell motility

The crucial role of substrate rigidity in regulating traction force and cytoskeletal organization prompted an investigation into cell motility on μPatterns. Utilizing SiR-actin, a fluorogenic and highly specific probe for F-actin in living cells [32], we tracked the migration of individual cells on 4 kPa and 20 kPa non-patterned substrates (Fig. 4A and B). Notably, the trajectories of randomly selected migrating cells exhibited an augmented migration activity specifically on 20 kPa substrates, a trend correlated with the effect of substrate rigidity on cell adhesion, cytoskeleton organization, and actomyosin-based contraction. Moreover, within confined monolayers, the cell density was observed to be higher in the central zones compared to the periphery, implying that cells in the core experienced larger compressive forces, thereby triggering myoblast fusion and differentiation [33].

Inspired by these findings, we delved into the migration behaviors of cells within specific zones on μPatterns. To this end, we meticulously tracked the individual cell movement in zone 1 of both 4 kPa and 20 kPa μPatterns (Fig. 4C and D). Remarkably, cells in zone 1 exhibited increased migration speed (1.94 ± 0.16 μm min^{-1}, Fig. 4E) along the longitudinal axis of the rectangular constraints compared to their counterparts on 4 kPa μPatterns, which migrated at a slower velocity (0.21 ± 0.07 μm min^{-1}, Fig. 4E) and with random directionality. Additionally, we compared the migration velocity of cells in zone 2 under both conditions. Cell migration appeared slower in zone 2 on both 4 kPa and 20 kPa μPatterns (Fig. 4F), indicating that cell motility is highly influenced by the topological constraints on μPatterns. One potential explanation is that cells experience compaction due to the crowding of cell populations, whereas cells at the periphery can migrate more freely due to less limitation of the adhered spaces. In addition, the acceleration of cell populations at the periphery potentially correlates with the constraints of μPatterns boundaries, as recently demonstrated to induce rotation flows in cell populations [16].

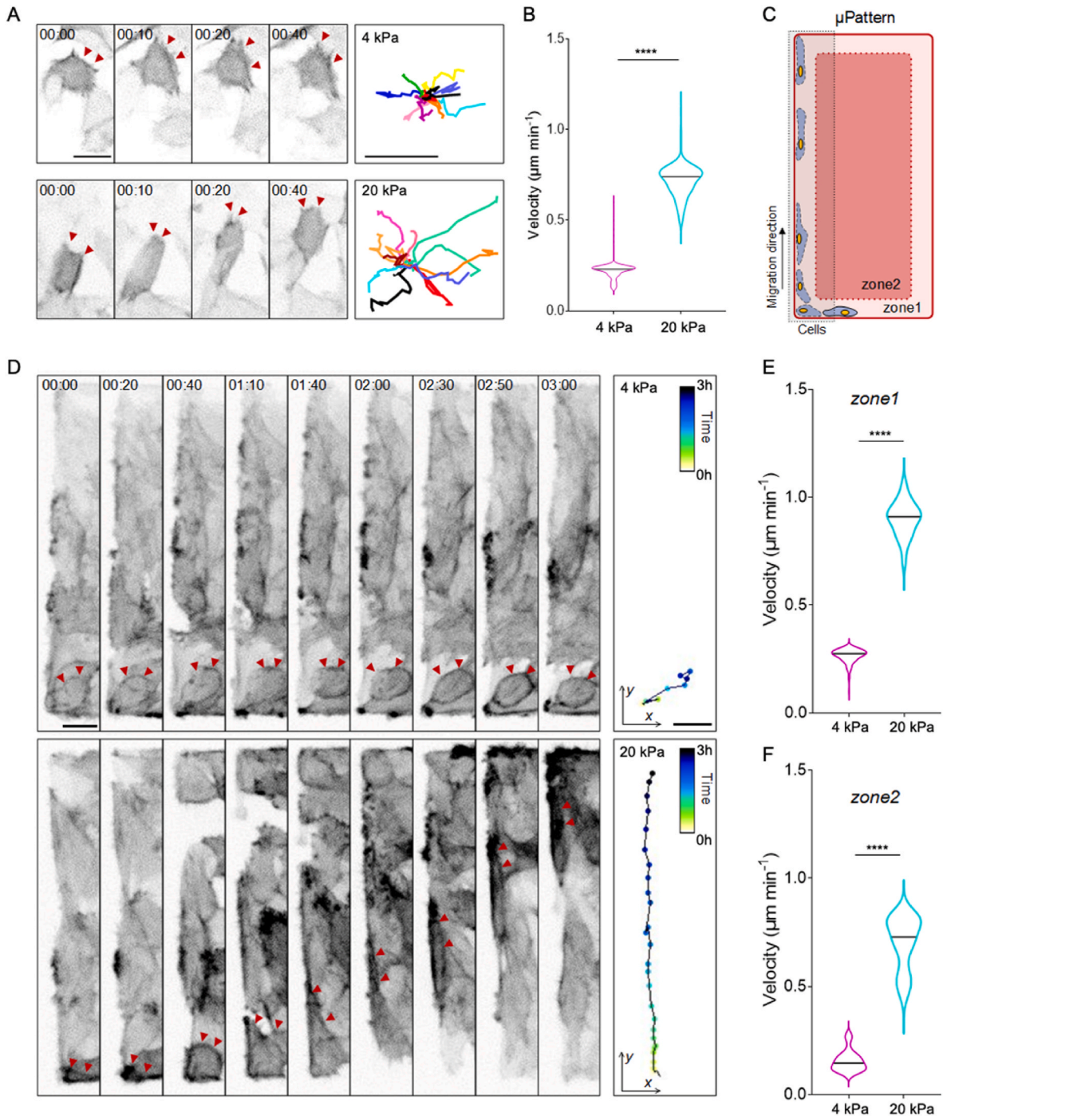

Fig. 4. Geometrical constraints regulate the individual cell migration. A) Time-lapse images of individual myoblasts labeled by SiR-actin on 4 kPa and 20 kPa substrates. The arrows indicate the cell leading edge. The far-right panels represent the trajectories of 11 randomly selected migrating cells for each condition. Times are indicated in h:min. Scale bars, 20 μm (cells) and 100 μm (trajectories). B) Cell migration velocity for myoblasts cultured on soft and stiff μPatterns. C) Illustration of the two different zones of individual μPatterns. The migration behaviors of cells in two zones were characterized (n > 100 cells from 10 μPatterns, N = 3 experiments). D) Time-lapse images of individual actin-labeled myoblasts in the zone 1 of either soft or stiff μPatterns. The far-right panels represent the corresponding trajectories of the migrating cells for each condition. Times are indicated in h:min. Scale bars, 20 μm. F, G) Cell migration velocity for myoblasts in zone 1 (F) and zone 2 (G) of soft and stiff μPatterns (n > 100 cells from 10 μPatterns, N = 3 experiments). The Kolmogorov–Smirnov test was used for data analysis. Data are presented as medians in violin graph (solid line).

2.4. Motility of cell populations at peripheral zones on μPatterns centripetally compact cells at the core

The tracking of individual cell migration provided insights into the migration behavior, revealing that cells migrate faster on 20 kPa μPatterns, an effect also influenced by the topological constraints. However, the overall global movement of cells remained unclear. To address this question, we extracted the average displacement field from phase-contrast videos of myoblasts on μPatterns using PIV (Fig. 5). We observed that except for the cells close to the μPattern edge (as shown in Fig. 4D), another cell population in the periphery could move towards the center region of μPatterns (Fig. 5A). For cells on 20 kPa μPatterns,

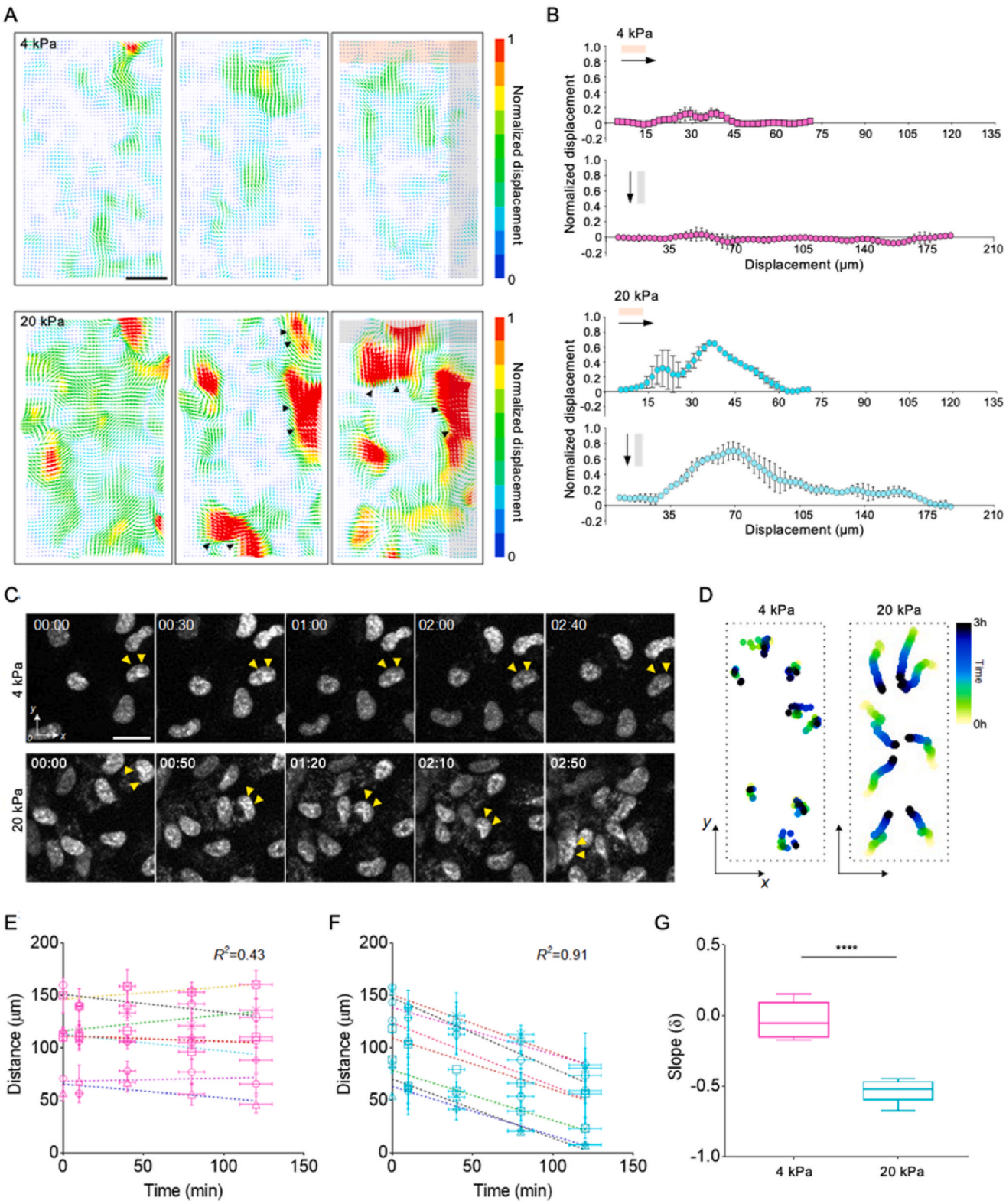

Fig. 5. Centripetal cell movement and crowding occur at stiff μPatterns. A) Displacement field of cell populations cultured on individual μPattern (up panel: soft, bottom panel: stiff, after 12 h seeding) by PIV analysis. The gray band indicated the zone 1 (periphery) on μPatterns. Scale bars, 20 μm. B) Normalized displacement as a function of dimensions of zone 1 (horizontal arrow indicates the width and perpendicular arrow indicates the length of zone 1) (n > μPatterns, N = 3 experiments). Data are presented as mean values ± s.d. C) Time-lapse images of nuclei (Hoechst 33342) in zone 2 of soft and stiff μPatterns. The gray band indicated zone 1 (pheriphery) on μPatterns. Scale bars, 10 μm. D) Color-coded trajectories of ~8 randomly selected nuclei in zone 2 (n = 8 nuclei, N = 2 experiments). E, F) Absolute distance between the nuclei and the geometrical center of μPattern plotted as a function of time on soft (E) and stiff (F) μPatterns (n = 10 nuclei, N = 2 experiments). G) The slope of the linear fit resutls of data in E and F. These results indicating a crowding effect of cell populations in zone 2. The Kolmogorov–Smirnov test was used for data analysis. Data are presented as mean values ± s.d. (For interpretation of the references to colour in this figure legend, the reader is referred to the Web version of this article.)

the amplitude of cell displacement increased with time at the periphery of μPatterns, whereas no such trend was observed at the core, indicating faster migration of cell populations closer to the μPattern boundaries. Conversely, the variations in the displacement field of cells on 4 kPa μPatterns were much lower in both the periphery and central zones, suggesting a relatively immobile cell population, consistent with the observations from individual cell tracking on μPatterns. Additionally, the peripheral cell populations migrated toward the core of μPatterns, indicating a global crowding of cell populations in the central zones. The locomotory capacity of cells is intricately linked to the fundamental properties of the actomyosin network, which can spontaneously polarize and generate directed forces [34]. These results suggest that the topological boundaries may accelerate the motility of cell populations at the periphery on stiff substrates, potentially correlated with increased levels of focal adhesion maturation and actomyosin-based contraction. Further investigation into these aspects should be conducted in subsequent studies. In vivo, myoblasts undergoing muscle regeneration typically migrate and display nuclei in their centers [35]. Consequently, we hypothesized that the acceleration of cell migration toward the central zones of μPatterns could induce the crowding of cell nuclei, subsequently triggering myoblast fusion. To test this hypothesis, we randomly tracked the nuclei positions of individual cells at the periphery of μPatterns (Fig. 5A and B). As anticipated, the timelapse images and trajectories of nuclei exhibited an obvious repositioning bias for cells on 4 kPa and 20 kPa substrates. This is further validated by plotting the distance between the center of the individual nucleus and the geometric center of μPatterns as a function of time (Fig. 5C–E). The distance curve shows a pronounced linearity, with an average slope of −0.53 for the nucleus on 20 kPa μPatterns, indicating a motion toward the core. In contrast, the slope is −0.03 for the nucleus on 4 kPa μPatterns, indicating a random directionality. All these results suggested that the enhanced regional cell migration and nucleus crowding depend on both topological constraints and rigidity of μPatterns. However, the underlying mechanism of nucleus crowding and movement should be investigated further.

2.5. The interplay between substrate rigidity and topological constraints induces myoblast differentiation

Cell elongation, alignment, and nuclei packing represent pivotal indicators both before and during myotube formation, a crucial process in myogenesis. In our model, the interplay of topological constraints and substrate rigidity significantly affects cell adhesion, elongation, and asymmetric population distribution through the migration and intracellular traction forces. Given these observations, we sought to investigate the potential impact of myoblast differentiation within our experimental model. Consequently, we assessed myoblast alignment, a morphological indicator closely associated with the initiation of myotube formation [15], by quantifying stress fiber orientation using the OrientationJ plugin. Remarkably, cells cultured on 20 kPa μPatterns exhibited robust alignment of stress fibers after 5 days of culturing, while such alignment significantly decreased in the absence of μPatterns (Fig. 6A and B). Conversely, no notable cell alignment was observed on 4 kPa substrates, with or without μPatterns. These findings suggest two important points: firstly, cell alignment is a synergistic outcome of substrate rigidity and topological constraints, and secondly, topological constraints may play a dominant role in this process. As cells undergo nuclear elongation during myotube formation, we quantified the aspect ratio of cell nuclei from immunostaining images (Fig. 6C). Notably, cells on 20 kPa μPatterns exhibited more elongated nuclei shapes compared to those on 4 kPa μPatterns, suggesting that myotube formation might occur subsequently.

To assess myotube formation on hydrogel substrates, with or without μPatterns, we conducted further experiments. For those cells on μPatterns, we mainly focus on the central region (zone 2) as it exhibits a crowding phenotype compared with the periphery. Remarkably, myotubes were not observed in cells cultured on 4 kPa substrates without μPatterns even after two weeks of culturing, as evidenced by the absence of myosin heavy chain (MyHC) expression, a specific indicator of myogenesis during myotube formation (Fig. 6D). Hence, it became evident that topological constraints alone could not trigger myotube formation in cells cultured on 4 kPa substrates. Intriguingly, myotube formation was more likely to occur on stiff substrates. The 3D reconstruction of representative z-stack images of myoblasts on 20 kPa gels revealed the morphology of individual myotubes, formed with multiple nuclei, suggestive of an early stage of myogenesis (Fig. 6E). Notably, myotube numbers were significantly increased on 20 kPa μPatterns, as indicated by the quantification of MyHC-positive area and the total number of nuclei fused within an individual myotube, respectively (Fig. 6F and G). In addition, myotube maturation on 20 kPa μPatterns was also evidenced by the sarcomere-like structures, identified by sarcomeric α-actinin in myoblasts culturing on 20 kPa μPatterns for 2 weeks (Supplementary Fig. 7). Collectively, these results strongly indicate that myotube formation is highly responsive to topological constraints only in the context of cells cultured on stiff substrates, thereby suggesting an intricate interplay between substrate rigidity and topological constraints in inducing myoblast differentiation.

3. Discussion

Our study highlights the biophysical pathway of cell elongation, alignment, and myotube formation guided by substrate rigidity and topological constraints. Using a PA-gel substrate with micropatterned adhesive proteins, we observed that myotube formation is strongly correlated to the interplay between substrate rigidity and topological constraints. Indeed, the cell adhesion and spreading are significantly enhanced on stiff μPatterns confirmed by quantifying the cell circularity, spreading area, and focal adhesion protein expression. To figure out the effect of topological constraints on cell spreading behavior, we characterized the cell circularity at different zones of μPatterns. Interestingly, the cells at the μPattern periphery showed an increased elongated shape compared with those at the core. Cell shape changes have been shown to correlate to its motile mode. During mesenchymal migration, cells showed elongated, spindle-like shapes with high-expressed focal adhesions and high actomyosin-based contractility [36]. This result, therefore, suggested a potential transition from a slow to fast mobile mode of cells on the periphery zones of μPatterns. To test this hypothesis, we further quantified the cell contractility on μPatterns through TFM. First, consistent with the results in the previous literature, elongated cells exhibited a more contractile phenotype on a stiff substrate. Second, we observed that the closer the cells are to the μPattern periphery, the greater their traction force, indicating a positive correlation between the position of the cells and their contractility.

In our system, we assumed that cell behavior and μPattern topology regulate each other. For example, as cells grow on μPatterns, the secretion of their own matrices and enzymatic degradation of environmental substrates may remodel the pattern and create dynamic feedbacks that regulate cellular migration. To this end, more robust high-resolution time-lapse imaging is necessary to explore how cells interact with μPatterns in the future.

A distinctive feature during myotube formation is a high level of cell elongation and ordered alignment. Moreover, the cell spreading is accompanied by stress fiber reorganization [37]. This motivated us to investigate the morphology of stress fibers in cells on μPatterns. Notably, cells cultured on 20 kPa μPatterns contain prolonged stress fibers that align parallelly to the longitude axis of μPatterns. On the contrary, the stress fibers are disordered and fragmented in the cells on 4 kPa μPatterns. These results suggested that actin reorganization is dependent on substrate rigidity. The variations of the cell shape on different zones on μPatterns lead us to test cell motility, which is highly linked to their spreading behaviors. We found a similar asymmetrical distribution of the cell migration on μPatterns. At the periphery, cells exhibit a faster

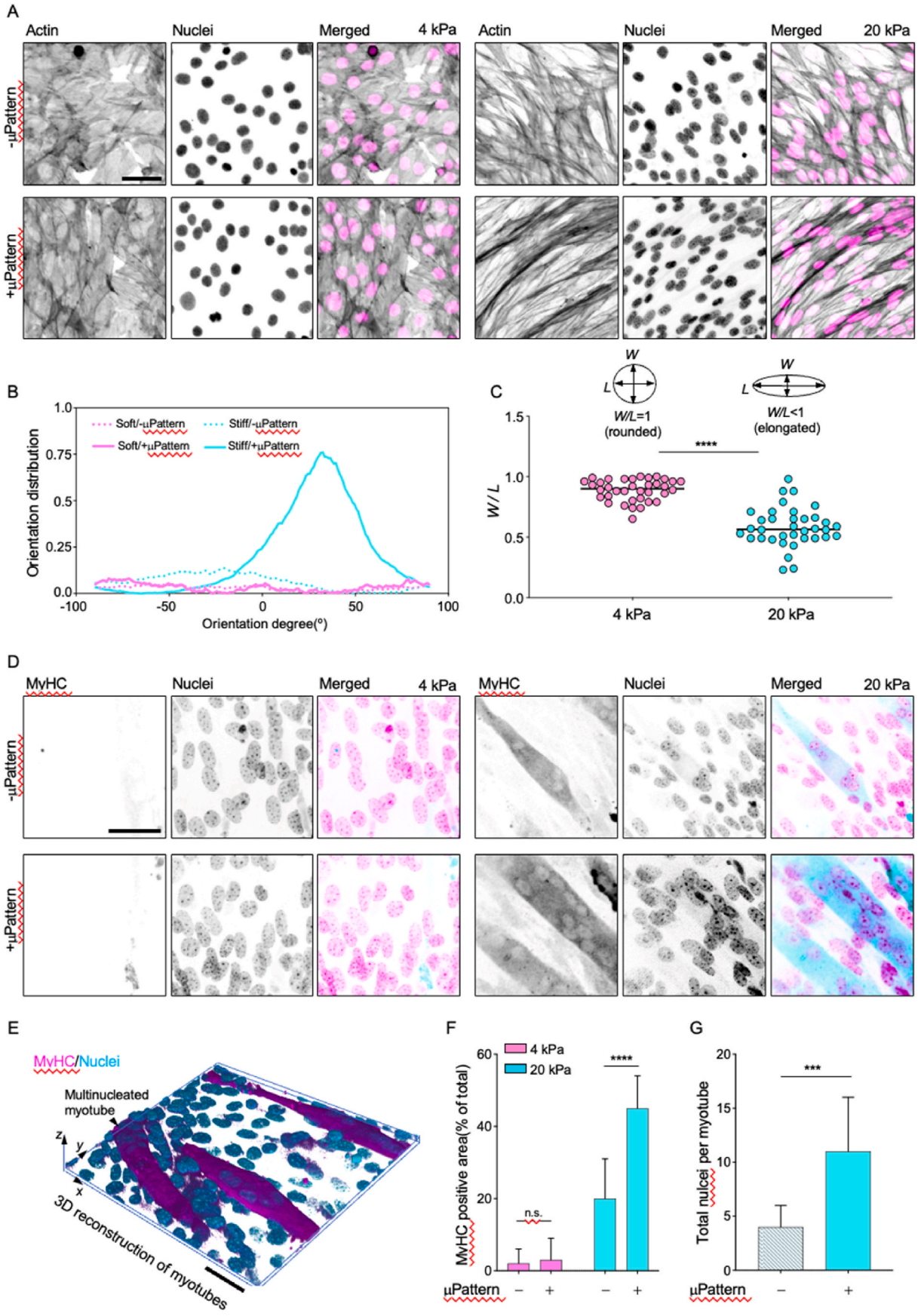

(caption on next page)

Fig. 6. The interplay of substrate rigidity and topological constraints on myoblast alignment and differentiation. A) Immunostaining images of actin (phalloidin) and nuclei (Hoechst) in myoblasts cultured on soft and stiff gel substrates with/without μPatterns. The experiments were conducted on day 5 of culturing. Scale bars, 10 μm. B) Orientation distribution of stress fibers in myoblasts (day 5) extracted from the confocal images (n = 10 samples, N = 3 experiments). The data were normalized from the sum of all values from multiple groups. C) Aspect ratio of cell nuclei on soft and stiff μPatterns on day 5 of culturing. D) Immunostaining images of MyHC (myosin 4) and nuclei (Hoechst) in myoblasts cultured on soft and stiff gel substrates with/without μPatterns. The experiments were conducted on 12 days of culturing. Scale bars, 10 μm. E) The 3D reconstruction of representative z-stack images showed the structure of myotube combining multiple nuclei on stiff μPatterns, suggesting an early stage of myogenesis. Scale bars, 5 μm. F) The ratio of the MyHC positive area (indicated by the MyHC fluorescence intensity) to the total area suggested the myotube formation at different conditions (n = 12 samples, N = 3 experiments). G) The total number of nuclei fused within an individual myotube for stiff gel substrate with/without μPatterns (n = 8 samples, N = 3 experiments).

motile mode with an elongated morphology, which is the opposite of cells at the core. This may be due to the different cell densities at the periphery and core zones of μPatterns. Limited by space constraints, cells in the core are unable to migrate rapidly. Tracking of Individual cell migration delivered the information that cells migrate faster on 20 kPa μPatterns, which is also regulated by the topological boundaries. However, the movement of cells in a global manner remains unclear. Therefore, we tested the cell population movement on μPatterns and observed that the cells at the core are compacted by the chiral movement of cells at the periphery of μPatterns. A potential explanation is that contractile interactions between cells and the topological constraints lead to cell elongation and lining up to give nematic ordering [16], resulting in active turbulence and contractile topological defects. Such defects have been found to correlate with the generation of force gradients and concentrate compressive stresses, which could also be a further test point to clarify the in-depth mechanism of myotube formation induced by the interplay between substrate rigidity and topological constraints. Myotube formation requires elongated, crowded, and highly aligned myoblasts, characteristics that our model effectively induces. Thus, we proceeded to examine myotube formation within our experimental setup. Interestingly, we observed a significant increase in myotube formation on stiff μPatterns, whereas, in the group without μPatterns, myotube formation was notably lower. This finding suggests that myotube formation is highly responsive to topological constraints in cells cultured on stiff substrates, indicating a complex interplay between substrate rigidity and topological constraints in inducing myoblast differentiation. However, underlying mechano-consequences of myotube formation in our model should be studied in the future. Firstly, the fusion of myotubes could be tested using live cell imaging or immunofluorescence with various myotube differentiation markers, such as Pax3 and Myf5 [38], particularly during the early stages of myogenesis. Secondly, the maturation of myotubes with multiple features, including hypertrophy, sarcomere structures, and relocalization of nuclei, warrants further exploration. Finally, the further functionality of myotube maturation should be tested in the future. For example, evaluating the contractility of fabricated myotubes in vitro by an electrical pulse stimulation.

In summary, our findings show that substrate rigidity and topological constraints regulate myoblast spreading, proliferation, migration, and localized differentiation. We conclude that the centripetal cellular mobile mode triggered by substrate rigidity and topological constraints results in compaction and crowding of central cells, which is a potential biophysical pathway to mediate myoblast differentiation and maturation.

4. Materials and methods

4.1. Preparation of Hydroxy-PA hydrogels

To constrain the cell spreading area, we micropatterned adhesive protein on polyacrylamide (PA) hydrogels, covalently bonded to glass slides, by using a microcontact printing method. To permit the immobilization of various ECM proteins, we chemically modified PA gels by incorporating hydroxyl-functionalized acrylamide monomers during the polymerization [25]. Before the hydrogel coating, the activation of cover slides is necessary. Briefly, the square coverslips (25 mm × 25 mm) were placed in a Petri dish and smeared with 0.1 M NaOH solution for 10 min in a chemical hood. The NaOH solution was then removed and fully immersed with sterile Milli-Q water for 20 min. Dry the coverslips gently under a steady flow of nitrogen gas and smear a thin layer of 3-(trimethoxysilyl) propyl acrylate (92 %) (475149, Sigma) on the activated side of the coverslip and leave it for at least 1 h. Then, the coverslips were rinsed 3 times with sterile Milli-Q water and stored at room temperature in a dry place with aluminum foil to avoid dust from sticking to the coverslips. Next, we prepared the hydroxy-PA gel by a reported protocol [39]. First, a weight of 65 mg of N-hydroxyethyl acrylamide (HEA) (697931, Sigma) in a 1.5 ml Eppendorf tube was prepared and then dissolved in 1 ml of 50 mM HEPES buffer. Second, 400 μL of acrylamide solution (40 % w/w in HEPES) was mixed with the specific volume of N,N′-methylenebis (acrylamide) (bis-Am) (146072, Sigma) solution (2 % w/w in HEPES) to reach the desired hydrogel rigidity (see Table 1). The solution is mixed using a vortexer and degassed in a vacuum chamber for 30 min to avoid oxygen within the solution, preventing hydroxy-PA gel polymerization. The solution was then sterilized by using a 0.2 μm pore size filter. In the meantime, the prepared cover slides were activated in a UV cleaner for 5 min. Third, 25 μl of 10 % ammonium persulfate (APS) (J76322, Thermo Fisher) solution and 2.5 μl of tetramethylenediamine (TEMED) (411019, Sigma) were added to the acrylamide/bis-acrylamide solution to trigger the polymerization. Finally, a 40 μl drop of the hydroxy- PA solution on the parafilm was rapidly and immediately covered with the activated face of the square glass coverslip for 20 min at room temperature. The coverslip with attached hydrogel was then separated carefully from the parafilm and then rinsed 3 times with PBS. The samples were then stored in PBS at 4 °C overnight to obtain full hydration before micropatterning.

4.2. Microstamp fabrication

Silicon molds were fabricated on silicon wafers using UV-photolithography and reactive ion etching. Next, polydimethylsiloxane (PDMS) (Sylgard®184, Dow Corning Corporation) and curing agent are mixed in a 10:1 ratio in a plastic beaker and mixed for 10 min. PDMS mixtures are placed into a vacuum environment to remove the air bubbles. Second, the microstructured silica matrices are placed in Petri dishes and casted into PDMS mixtures with 15 mm thickness and curved overnight 70 °C. The PDMS layer is then gently peeled off from the silica matrices and cutted as 1 cm2 PDMS stamps using a scalpel. Then, all the microstamp pattern is cleaned using adhesive tapes and upwards in the Petri dish.

Table 1
Fabrication of hydroxy-PAAm hydrogels with various rigidities.

HEA (μl)	Acrylamide 40 % (μl)	Bis-Am 2 % (μl)	HEPES (μl)	Mean Young's modulus (kPa)
1065	400	150	3385	4.26
1065	400	250	3285	9.28
1065	400	400	3135	12.25
1065	400	600	2935	22.23

4.3. μPatterns preparation

Before micropatterning, PDMS stamps were cleaned in 70 % w/w ethanol and sonicated for 30 min. The stamps were then dried with a nitrogen stream and placed in a UV cleaner for 5 min. A 200 μL drop of fibronectin solution (15 μg/ml in PBS) (33016015, Thermo Fisher) onto the microstructured surface of the PDMS stamp for 1 h at room temperature. The hydrogel samples were removed from PBS and gently dried by a low nitrogen stream. The structured surface of PDMS was also dried by nitrogen flow and placed in contact with the hydrogel surface. The PDMS stamp was then slightly pressed with the tip of a tweezer to ensure intense contact between the stamp microstructures and the hydrogel surface. The PDMS stamp was kept on the hydrogel for 1 h at room temperature and gently removed. The hydrogel with μPatterns were rinsed gently with PBS three times and passivated with 10 mg/ml bovine serum albumin (BSA, 9048, Sigma) at 4 °C overnight. The passivated samples were rinsed three times with PBS and could be stored at 4 °C at least for 3 days before use.

4.4. Cell seeding and differentiation

C2C12 myoblasts (ATCC) were grown with DMEM medium supplemented with 10 % fetal bovine serum (FBS) (Life Technologies) and 1 % penicillin-streptomycin (5140122, Thermo Fisher) at 37 °C, and 5 % CO2. Micropatterned coverslips were incubated in a culture medium for 15 min before plating cells. 1 ml of the cell suspension (density 2×10^4 cells/ml) was added on each cover slide, then placed in an incubator for 20 min. Next, the cover slide was rinsed once by a culture medium to remove the non-adherent cells and placed in the incubator for 3 h to spread fully. For the myoblast differentiation, a differentiation media with 2 % horse serum which was exchanged on day 3 after cell seeding.

4.5. Atomic force microscopy

The rigidity of hydroxy-PA hydrogel was tested using atomic force microscopy (AFM, Agilent 5500) through nano-indentation. Hydrogels on 35 mm dishes were swollen to equilibrium in PBS and indented at a velocity of 10 μm s^{-1}. Before and during indentation experiments, hydrogels were kept in PBS. Rigidity from force curves was obtained using the NanoScope Analysis software, correcting for baseline tilt using the linear fitting option with the Hertz model described previously.

$$F = \frac{2}{\pi} \times \frac{E}{1-\nu^2} \times \tan\alpha \times \delta$$

Young's modulus was computed using the Hertz model described previously (Roduit et al., 2008). where F represents the indentation force, E is the Young's modulus to be determined, u is the Poisson ratio of the materials (we set its value as 0.5), $\boldsymbol{\alpha}$ is the half opening angle of the tip (here is 35°), and $\boldsymbol{\delta}$ is the indentation depth.

4.6. Characterization of swelling property of Hydroxy-PA gels

Approximately 0.3 g of the hydrogel samples with a grain size of 0.15–0.3 mm was placed in 1 mL PBS at room temperature for a specified time. During this time, the suspension was gently stirred. Subsequently, the unbound PBS was quickly removed by filtering through a stainless-steel sieve with a mesh size of 0.5 mm. The samples were weighed. Measurements were repeated three times for each sample. The swelling ratio (%) was calculated from Equation:

$$W = \frac{M_w - M_d}{M_d} \times 100$$

where: W is the swelling ratio at time t, M_w (g) is weight of swollen gel at time t, and M_d (g) is the weight of dry gel.

4.7. Traction force microscopy

TFM was performed as described previously (Dembo and Wang, 1999). The displacement fields of embedded fluorescent microspheres (0.2 μm red fluorescent microspheres, ~5.0×10^8/ml final concentration, F8811, Invitrogen) of hydrogels were obtained from z-stack microscope images (actin labeled with phalloidin) before and after removal of cells by trypsin treatment. The images were paired and aligned to correct for experimental drift and then calculated by a ImageJ plugin. Final vector-grid size ranged from 1.2 μm × 1.2 μm–1.6 μm × 1.6 μm according to the magnification. Traction force field was subsequently reconstructed by Fourier-transform traction cytometry. The background of the measurements was estimated by analyzing three fields (without cells) of view per substrate rigidity.

4.8. Actin orientation, cell migration, and nuclei tracking

The manual tracking plugin (Trackmate) for ImageJ was used to manually track trajectories of cells. Particle image velocimetry analysis of the flows in either cell populations or nuclei on μPatterns was performed with an open source 2D PIV program based on Java script (JPIV). In particular, we used the (basic) iterative PIV with two passes, with decreasing interrogation window size (20 × 20 μm and 10 × 10 μm, respectively), which show good qualitative agreement with our experimental observations. Temporal resolution was set to a minimum of 5 or 10 min between frames.

4.9. Immunofluorescence and labelling

Cells were fixed in 0.5 % glutaraldehyde (111308, Sigma) and 2 % paraformaldehyde (30525, Sigma) in cytoskeleton buffer 10 % sucrose pH 6.1 for 20 min at room temperature. Cells were then rinsed three times with PBS and blocked with 2 % BSA at 4 °C overnight. The cells were incubated with appropriate dilutions of primary antibodies in PBS for 1 h at 4 °C in a humid chamber and rinsed three times with PBS. The coverslips were then incubated with secondary antibodies diluted in PBS for 30 min at room temperature in a humid chamber and rinsed three times with PBS. The myosin 4 monoclonal antibody conjugated with eFluor™ 660 (MF20, Thermo Fisher) was used (1:400 dilution) for MyHC labelling. The Total microtubules were labeled using alpha tubulin monoclonal antibody (1:500 dilution, MA180017, Invitrogen) and Alexa Fluor™ 488 secondary antibody (1:500 dilution, anti-Rat, A21208, Invitrogen). For actin labelling, Phalloidin (Alexa Fluor™ 555, A34055, Thermo Fisher) was used (1:500 dilution). The sarcomeric Z-disk in myotube was identified using anti-α-actinin (sarcomeric) antibody (A7732, Sigma, 1:800 dilution). The cell nuclei were visualized either by DAPI (500 nM, Sigma, D9542) or Hoechst 33342 (10 μM) for live imaging. The cells were mounted onto slides with Mowiol® 18–88 gelvatol (Sigma) overnight before imaging. SiR-actin was used for actin structures labeling in myoblasts during live imaging. Briefly, 200 nM SiR-actin was diluted from a 1 mM stock solution in cell culture medium. Meanwhile, 10 μM verapamil was added to inhibit efflux pumps. The myoblasts were then incubated with SiR-actin and verapamil mixture for 6 h before live imaging.

4.10. Imaging

Time-lapse imaging was performed with an inverted microscope Nikon Ti-E installed into a thermostatically controlled chamber (Life Imaging Technologies) and equipped with a micro-incubator for thermal, CO2 and humidity control (Okolab). The microscope was also equipped with an automated stage and a Yokogawa CSU-W1 spinning disc unit. Image acquisition was performed with an Andor Zyla 4.2 Plus camera, operated with Slidebook (v.6.0.19). We performed fluorescence (× 60 lens, NA 1.4), phase-contrast (× 10/ × 20 objectives, NA 0.3/0.45) and differential interference contrast imaging (× 20 lens, NA

0.45). Four-dimensional time-lapse was used for actin-labeled cell mounds (× 60 lens, NA 1.4) and for the pillar compression experiments. The latter combined differential interference contrast and confocal fluorescence modes (× 20 lens, NA 0.45). Typically, we acquired either 6 or 12 images per hour for >10 h.

4.11. Statistics

All the reported results were obtained from experiments repeated independently 2–3 times in different conditions. Quantification always considered measurements from several μPatterns (n, indicated in the figure legends). For fixed samples, we considered >10 μPatterns to be sufficient for the statistical analyses. For comparison of continuous variables across multiple groups, the statistical significance was analyzed by one-way ANOVA with Tukey post-hoc testing using GraphPad Prism 9 (GraphPad Software). Significance levels were set at *$p < 0.05$, **$p < 0.01$, ***$p < 0.001$, and ****$p < 0.0001$.

Funding

This work was supported by the National Natural Science Foundation of China (81970960, 82001079), International cooperation plan project of Shaanxi (S2024-YF-GHMS-0071) , the CSA Clinical Research Fund (CSA-02022-01), the National Clinical Research Center for Oral Diseases (LCB202202), the Key Research and Development Program of Shaanxi Province (2022SF-227), and the Natural Science Foundation of Shannxi Province (2020JM-321).

CRediT authorship contribution statement

Jie Gao: Writing – review & editing, Visualization, Software, Resources, Methodology, Investigation, Formal analysis, Data curation, Conceptualization. **Xiang Sun:** Writing – review & editing, Visualization, Software, Resources, Project administration, Methodology, Investigation. **Yanning Ma:** Visualization, Project administration, Methodology, Investigation. **Wen Qin:** Resources, Methodology, Investigation, Funding acquisition, Data curation. **Jin Li:** Visualization, Resources, Methodology, Investigation. **Zuolin Jin:** Writing – review & editing, Writing – original draft, Visualization, Investigation. **Jun Qiu:** Writing – review & editing, Writing – original draft, Visualization, Validation, Supervision, Methodology, Investigation, Data curation, Conceptualization. **Hao Zhang:** Writing – review & editing, Writing – original draft, Visualization, Validation, Supervision, Resources, Methodology, Investigation, Funding acquisition, Conceptualization.

Declaration of competing interest

The authors declare that they have no known competing financial interests or personal relationships that could have appeared to influence the work reported in this paper.

Data availability

Data will be made available on request.

Appendix A. Supplementary data

Supplementary data to this article can be found online at https://doi.org/10.1016/j.mtbio.2024.101195.

References

[1] D.S. Gokhin, V.M. Fowler, A two-segment model for thin filament architecture in skeletal muscle, Nat. Rev. Mol. Cell Biol. 14 (2013), https://doi.org/10.1038/nrm3510.
[2] J.M. Hernández-Hernández, E.G. García-González, C.E. Brun, M.A. Rudnicki, The myogenic regulatory factors, determinants of muscle development, cell identity and regeneration, Semin. Cell Dev. Biol. 72 (2017), https://doi.org/10.1016/j.semcdb.2017.11.010.
[3] J. Menetrey, C. Kasemkijwattana, C.S. Day, P. Bosch, M. Vogt, F.H. Fu, M. S. Moreland, J. Huard, Growth factors improve muscle healing in vivo, J. Bone. Joint. Surg. Br. 82-B (2000), https://doi.org/10.1302/0301-620x.82b1.0820131.
[4] S. Chargé, M.A. Rudnicki, Fusion with the fused: a new role for interleukin-4 in the building of muscle, Cell 113 (2003), https://doi.org/10.1016/S0092-8674(03)00358-1.
[5] M. Yu, H. Wang, Y. Xu, D. Yu, D. Li, X. Liu, W. Du, Insulin-like growth factor-1 (IGF-1) promotes myoblast proliferation and skeletal muscle growth of embryonic chickens via the PI3K/Akt signalling pathway, Cell Biol. Int. 39 (2015), https://doi.org/10.1002/cbin.10466.
[6] B.C. Syverud, K.W. VanDusen, L.M. Larkin, Growth factors for skeletal muscle tissue engineering, Cells Tissues Organs 202 (2016), https://doi.org/10.1159/000444671.
[7] S.E. Chen, B. Jin, Y.P. Li, TNF-α regulates myogenesis and muscle regeneration by activating p38 MAPK, Am. J. Physiol. Cell Physiol. 292 (2007), https://doi.org/10.1152/ajpcell.00486.2006.
[8] M. Hoene, H. Runge, H.U. Häring, E.D. Schleicher, C. Weigert, Interleukin-6 promotes myogenic differentiation of mouse skeletal muscle cells: role of the STAT3 pathway, Am. J. Physiol. Cell Physiol. 304 (2013), https://doi.org/10.1152/ajpcell.00025.2012.
[9] N.M. Luis, F. Schnorrer, Mechanobiology of muscle and myofibril morphogenesis, Cells Dev. 168 (2021), https://doi.org/10.1016/j.cdev.2021.203760.
[10] C. Vesga-Castro, J. Aldazabal, A. Vallejo-Illarramendi, J. Paredes, Contractile force assessment methods for in vitro skeletal muscle tissues, Elife 11 (2022), https://doi.org/10.7554/eLife.77204.
[11] A.J. Engler, M.A. Griffin, S. Sen, C.G. Bönnemann, H.L. Sweeney, D.E. Discher, Myotubes differentiate optimally on substrates with tissue-like stiffness: pathological implications for soft or stiff microenvironments, JCB (J. Cell Biol.) 166 (2004), https://doi.org/10.1083/jcb.200405004.
[12] A. Kumar, R. Murphy, P. Robinson, L. Wei, A.M. Boriek, Cyclic mechanical strain inhibits skeletal myogenesis through activation of focal adhesion kinase, Rac-1 GTPase, and NF-kB transcription factor, Faseb. J. 18 (2004), https://doi.org/10.1096/fj.04-2414com.
[13] H.H. Vandenburgh, J. Shansky, R. Solerssi, J. Chromiak, Mechanical stimulation of skeletal muscle increases prostaglandin F2α production, cyclooxygenase activity, and cell growth by a pertussis toxin sensitive mechanism, J. Cell. Physiol. 163 (1995), https://doi.org/10.1002/jcp.1041630209.
[14] C.P. Pennisi, C.G. Olesen, M. De Zee, J. Rasmussen, V. Zachar, Uniaxial cyclic strain drives assembly and differentiation of skeletal myocytes, Tissue Eng. 17 (2011), https://doi.org/10.1089/ten.tea.2011.0089.
[15] Y. Li, G. Huang, X. Zhang, L. Wang, Y. Du, T.J. Lu, F. Xu, Engineering cell alignment in vitro, Biotechnol. Adv. 32 (2014), https://doi.org/10.1016/j.biotechadv.2013.11.007.
[16] P. Guillamat, C. Blanch-Mercader, G. Pernollet, K. Kruse, A. Roux, Integer topological defects organize stresses driving tissue morphogenesis, Nat. Mater. 21 (2022), https://doi.org/10.1038/s41563-022-01194-5.
[17] J.L. Charest, A.J. García, W.P. King, Myoblast alignment and differentiation on cell culture substrates with microscale topography and model chemistries, Biomaterials 28 (2007), https://doi.org/10.1016/j.biomaterials.2007.01.020.
[18] S. Alom Ruiz, C.S. Chen, Microcontact printing: a tool to pattern, Soft Matter 3 (2007) 168–177, https://doi.org/10.1039/B613349E.
[19] C.S. Chen, M. Mrksich, S. Huang, G.M. Whitesides, D.E. Ingber, Micropatterned surfaces for control of cell shape, position, and function, Biotechnol. Prog. 14 (1998) 356–363, https://doi.org/10.1021/bp980031m.
[20] B.B. O'Connor, T. Grevesse, J.F. Zimmerman, H.A.M. Ardoña, J.A. Jimenez, D. Bitounis, P. Demokritou, K.K. Parker, Human brain microvascular endothelial cell pairs model tissue-level blood–brain barrier function, Integr. Biol. 12 (2020) 64–79, https://doi.org/10.1093/intbio/zyaa005.
[21] K. Daliri, K. Pfannkuche, B. Garipcan, Effects of physicochemical properties of polyacrylamide (PAA) and (polydimethylsiloxane) PDMS on cardiac cell behavior, Soft Matter 17 (2021) 1156–1172, https://doi.org/10.1039/D0SM01986K.
[22] M. Luciano, S.-L. Xue, W.H. De Vos, L. Redondo-Morata, M. Surin, F. Lafont, E. Hannezo, S. Gabriele, Cell monolayers sense curvature by exploiting active mechanics and nuclear mechanoadaptation, Nat. Phys. 17 (2021) 1382–1390, https://doi.org/10.1038/s41567-021-01374-1.
[23] N. Jiwlawat, E.M. Lynch, B.N. Napiwocki, A. Stempien, R.S. Ashton, T.J. Kamp, W. C. Crone, M. Suzuki, Micropatterned substrates with physiological stiffness promote cell maturation and Pompe disease phenotype in human induced pluripotent stem cell-derived skeletal myocytes, Biotechnol. Bioeng. 116 (2019) 2377–2392, https://doi.org/10.1002/bit.27075.
[24] A.B. Mathur, A.M. Collinsworth, W.M. Reichert, W.E. Kraus, G.A. Truskey, Endothelial, cardiac muscle and skeletal muscle exhibit different viscous and elastic properties as determined by atomic force microscopy, J. Biomech. 34 (2001) 1545–1553, https://doi.org/10.1016/S0021-9290(01)00149-X.
[25] T. Grevesse, M. Versaevel, G. Circelli, S. Desprez, S. Gabriele, A simple route to functionalize polyacrylamide hydrogels for the independent tuning of mechanotransduction cues, Lab Chip 13 (2013), https://doi.org/10.1039/c2lc41168g.
[26] M.A. Wozniak, C.S. Chen, Mechanotransduction in development: a growing role for contractility, Nat. Rev. Mol. Cell Biol. 10 (2009), https://doi.org/10.1038/nrm2592.
[27] J.D. Humphries, P. Wang, C. Streuli, B. Geiger, M.J. Humphries, C. Ballestrem, Vinculin controls focal adhesion formation by direct interactions with talin and actin, JCB (J. Cell Biol.) 179 (2007), https://doi.org/10.1083/jcb.200703036.

[28] K. Ren, T. Crouzier, C. Roy, C. Picart, Polyelectrolyte multilayer films of controlled stiffness modulate myoblast cell differentiation, Adv. Funct. Mater. 18 (2008), https://doi.org/10.1002/adfm.200701297.
[29] S.A. Maskarinec, C. Franck, D.A. Tirrell, G. Ravichandran, Quantifying cellular traction forces in three dimensions, Proc. Natl. Acad. Sci. USA 106 (2009) 22108–22113, https://doi.org/10.1073/pnas.0904565106.
[30] S. Munevar, Y. Wang, M. Dembo, Traction force microscopy of migrating normal and H-ras transformed 3T3 fibroblasts, Biophys. J. 80 (2001) 1744–1757, https://doi.org/10.1016/S0006-3495(01)76145-0.
[31] S.Y. Tee, J. Fu, C.S. Chen, P.A. Janmey, Cell shape and substrate rigidity both regulate cell stiffness, Biophys. J. 100 (2011), https://doi.org/10.1016/j.bpj.2010.12.3744.
[32] G. Lukinavičius, L. Reymond, E. D'Este, A. Masharina, F. Göttfert, H. Ta, A. Güther, M. Fournier, S. Rizzo, H. Waldmann, C. Blaukopf, C. Sommer, D.W. Gerlich, H. D. Arndt, S.W. Hell, K. Johnsson, Fluorogenic probes for live-cell imaging of the cytoskeleton, Nat. Methods 11 (2014), https://doi.org/10.1038/nmeth.2972.
[33] R. Tran, C. Moraes, C.A. Hoesli, Controlled clustering enhances PDX1 and NKX6.1 expression in pancreatic endoderm cells derived from pluripotent stem cells, Sci. Rep. 10 (2020), https://doi.org/10.1038/s41598-020-57787-0.
[34] M.L. Gardel, I.C. Schneider, Y. Aratyn-Schaus, C.M. Waterman, Mechanical integration of actin and adhesion dynamics in cell migration, Annu. Rev. Cell Dev. Biol. 26 (2010), https://doi.org/10.1146/annurev.cellbio.011209.122036.
[35] C.H. Hakim, N.B. Wasala, X. Pan, K. Kodippili, Y. Yue, K. Zhang, G. Yao, B. Haffner, S.X. Duan, J. Ramos, J.S. Schneider, N.N. Yang, J.S. Chamberlain, D. Duan, A five-repeat micro-dystrophin gene ameliorated dystrophic phenotype in the severe DBA/2J-mdx model of duchenne muscular dystrophy, Mol. Ther. Methods Clin. Dev. 6 (2017) 216–230, https://doi.org/10.1016/j.omtm.2017.06.006.
[36] M. Murrell, P.W. Oakes, M. Lenz, M.L. Gardel, Forcing cells into shape: the mechanics of actomyosin contractility, Nat. Rev. Mol. Cell Biol. 16 (2015), https://doi.org/10.1038/nrm4012.
[37] A. Zemel, F. Rehfeldt, A.E.X. Brown, D.E. Discher, S.A. Safran, Cell shape, spreading symmetry, and the polarization of stress-fibers in cells, J. Phys. Condens. Matter 22 (2010), https://doi.org/10.1088/0953-8984/22/19/194110.
[38] J. Chal, O. Pourquié, Making muscle: skeletal myogenesis in vivo and in vitro, Development (Camb.) (2017) 144, https://doi.org/10.1242/dev.151035.
[39] T. Grevesse, M. Versaevel, S. Gabriele, Preparation of Hydroxy-PAAm hydrogels for decoupling the effects of mechanotransduction cues, JoVE (2014), https://doi.org/10.3791/51010.